Synthetic aperture focusing technique for photoacoustic endoscopy

DE CAI,[1] GUANGYAO LI,[1] DONGQING XIA,[1] ZHONGFEI LI,[1] ZHENDONG GUO,[1] AND SUNG-LIANG CHEN[1,2,*]

[1]*University of Michigan-Shanghai Jiao Tong University Joint Institute, Shanghai Jiao Tong University, Shanghai 200240, China*
[2]*State Key Laboratory of Advanced Optical Communication Systems and Networks, Shanghai Jiao Tong University, Shanghai 200240, China*
sungliang.chen@sjtu.edu.cn

Abstract: Photoacoustic endoscopy (PAE) is a promising tool for the detection of atherosclerotic plaque. In this work, we propose a novel design of a side-viewing PAE probe based on a synthetic aperture focusing technique (SAFT) to enable high transverse resolution over large depth of focus (DOF) along the radial direction. A point-like ultrasonic detector is used to ensure a wide detection angle and thus a large synthetic aperture for SAFT. We first perform numerical simulation to optimize the PAE probe design, which involves the placement of the point-like detector and the diameter of a reflection rod mirror. Then, experiments are conducted based on the optimized probe design. High transverse resolution of 115–190 μm over large DOF of 3.5 mm along the radial direction is experimentally obtained. The SAFT-based PAE holds promise for endoscopic imaging with a high transverse resolution for both the surface and deep regions of tissue.

OCIS codes: (170.3880) Medical and biological imaging; (170.5120) Photoacoustic imaging; (170.2150) Endoscopic imaging; (100.0100) Image processing.

References and links

1. S. Tang, J. Chen, P. Samant, S. Kelly, and L. Xiang, "Transurethral photoacoustic endoscopy for prostate cancer: A simulation study," IEEE Trans. Med. Imaging **35**(7), 1780–1787 (2016).
2. J.-M. Yang, C. Favazza, R. Chen, J. Yao, X. Cai, K. Maslov, Q. Zhou, K. K. Shung, and L. V. Wang, "Simultaneous functional photoacoustic and ultrasonic endoscopy of internal organs in vivo," Nat. Med. **18**(8), 1297–1302 (2012).
3. C. Chen, Y. Zhao, S. Yang, and D. Xing, "Mechanical characterization of intraluminal tissue with phase-resolved photoacoustic viscoelasticity endoscopy," Biomed. Opt. Express **6**(12), 4975–4980 (2015).
4. S. Sethuraman, S. R. Aglyamov, J. H. Amirian, R. W. Smalling, and S. Y. Emelianov, "Intravascular photoacoustic imaging using an IVUS imaging catheter," IEEE Trans. Ultrason. Ferroelectr. Freq. Control **54**(5), 978–986 (2007).
5. B. Wang, J. L. Su, J. Amirian, S. H. Litovsky, R. Smalling, and S. Emelianov, "Detection of lipid in atherosclerotic vessels using ultrasound-guided spectroscopic intravascular photoacoustic imaging," Opt. Express **18**(5), 4889–4897 (2001).
6. K. Jansen, A. F. Van Der Steen, H. M. van Beusekom, J.W. Oosterhuis, and G. van Soest, "Intravascular photoacoustic imaging of human coronary atherosclerosis," Opt. Lett. **36**(5), 597–599 (2011).
7. X. Bai, X. Gong, W. Hau, R. Lin, J. Zheng, C. Liu, C. Zeng, X. Zou, H. Zheng, and L. Song, "Intravascular optical-resolution photoacoustic tomography with a 1.1 mm diameter catheter," PloS one **9**(3), e92463 (2014).
8. J.-M. Yang, C. Li, R. Chen, B. Rao, J. Yao, C.-H. Yeh, A. Danielli, K. Maslov, Q. Zhou, K. K. Shung and L. V. Wang, "Optical-resolution photoacoustic endomicroscopy in vivo," Biomed. Opt. Express **6**(3), 918–932 (2015).
9. J.-M. Yang, K. Maslov, H.-C. Yang, Q. Zhou, K. K. Shung, and L. V. Wang, "Photoacoustic endoscopy," Opt. Lett. **34**(10), 1591–1593 (2009).
10. J.-M. Yang, R. Chen, C. Favazza, J. Yao, C. Li, Z. Hu, Q. Zhou, K. K. Shung, and L. V. Wang, "A 2.5-mm diameter probe for photoacoustic and ultrasonic endoscopy," Opt. Express **20**(21), 23944–23953 (2012).
11. H. He, G. Wissmeyer, S.V. Ovsepian, A. Buehler and V. Ntziachristos, "Hybrid optical and acoustic resolution optoacoustic endoscopy," Opt. Lett. **41**(12), 2708–2710 (2016).
12. B. Dong, S. Chen, Z. Zhang, C. Sun, and H. F. Zhang, "Photoacoustic probe using a microring resonator ultrasonic sensor for endoscopic applications," Opt. Lett. **39**(15), 4372–4375 (2014).
13. C.-K. Liao, M.-L. Li, and P.-C. Li, "Optoacoustic imaging with synthetic aperture focusing and coherence weighting," Opt. Lett. **29**(21), 2506–2508 (2004).
14. M.-L. Li, H. F. Zhang, K. Maslov, G. Stoica, and L. V. Wang, "Improved in vivo photoacoustic microscopy based on a virtual-detector concept," Opt. Lett. **31**(4), 474–476 (2006).

15. D. Cai, Z. Li, and S.-L. Chen, "Photoacoustic microscopy by scanning mirror-based synthetic aperture focusing technique," Chin. Opt. Lett. **13**(10), 101101 (2015).
16. M. O'Donnell and L. Thomas, "Efficient synthetic aperture imaging from a circular aperture with possible application to catheter-based imaging," IEEE Trans. Ultrason. Ferroelectr. Freq. Control **39**(3), 366–380 (1992).
17. X. Chen, M. Li, Y. Li, Y. Wang, and D. Yu, "Synthetic aperture focusing for medical endoscopic ultrasonography," J. X-Ray Sci. Technol. **19**(1), 127–137 (2011).
18. C. Sheaff and S. Ashkenazi, "A fiber optic optoacoustic ultrasound sensor for photoacoustic endoscopy," in *Proceedings of IEEE Conference on Ultrasonics* (Institute of Electrical and Electronics Engineers, New York, 2010), pp. 2135–2138.
19. E. Z. Zhang and P. C. Beard, "A miniature all-optical photoacoustic imaging probe," Proc. SPIE **7899**, 78990 (2011).
20. P. Morris, A. Hurrell, and P. Beard , "Development of a 50 MHz fabry-perot type fibre-optic hydrophone for the characterisation of medical ultrasound fields," in *Proceedings* (Institute of Acoustics, St Albans, 2006), pp. 717–725.
21. G. Diebold, T. Sun, and M. Khan, "Photoacoustic monopole radiation in one, two, and three dimensions," Phys. Rev. Lett. **67**(24), 3384 (1991).
22. S.-L. Chen, T. Ling, and L. J. Guo, "Low-noise small-size microring ultrasonic detectors for high-resolution photoacoustic imaging," J. Biomed. Opt. **16**(5), 056001 (2011).
23. M. Xu, Y. Xu, and L. V.Wang, "Time-domain reconstruction algorithms and numerical simulations for thermoacoustic tomography in various geometries," IEEE Trans. Biomed. Eng. **50**(9), 1086–1099 (2003).
24. D. T. Blackstock, *Fundamentals of Physical Acoustics* (John Wiley & Sons, 2000).
25. J. M. Cannata, J. A. Williams, Q. Zhou, T. A. Ritter, and K. K. Shung, "Development of a 35-MHz piezo-composite ultrasound array for medical imaging," IEEE Trans. Ultrason. Ferroelectr. Freq. Control **53**(1), 224–236 (2006).
26. T. J. Allen, E. Zhang, and P. C. Beard, "Large-field-of-view laser-scanning OR-PAM using a fibre optic sensor," Proc. SPIE **93230**, 932301 (2015).
27. T. Ling, S.-L. Chen, and L. J. Guo, "High-sensitivity and wide-directivity ultrasound detection using high Q polymer micro-ring resonators," Appl. Phys. Lett. **98**(20), 204103 (2011).
28. C. Zhang, T. Ling, S.-L. Chen, and L. J. Guo, "Ultrabroad bandwidth and highly sensitive optical ultrasonic detector for photoacoustic imaging," ACS Photonics **1**(11), 1093–1098 (2014).
29. H. Andresen, S. I. Nikolov, and J. A. Jensen, "Synthetic aperture focusing for a single-element transducer undergoing helical motion," IEEE Trans. Ultrason. Ferroelectr. Freq. Control **58**(5), 935–943 (2011).

1. Introduction

Photoacoustic endoscopy (PAE) combining the advantages of high optical contrast and high ultrasound imaging depth has found various biomedical applications [1–3], especially for imaging atherosclerotic plaque [4–6]. High-resolution imaging enables detection of small plaques, which is essential for early diagnosis of atherosclerosis and thus, is of important clinical value. High resolution can be provided either by optical focusing, termed as optical-resolution PAE (OR-PAE) or acoustic focusing, termed as acoustic-resolution PAE (AR-PAE). OR-PAE [7, 8] can achieve high resolution of several micrometers. However, the penetration depth is limited to ~1 mm in biological tissue. AR-PAE has the advantage of high ultrasound penetration depth using either an unfocused or focused transducer [9–12]. The use of the unfocused transducer suffers from poor transverse resolution, especially for deep tissue imaging. Although the focused transducer with high numerical aperture (NA) can provide high transverse resolution, depth of focus (DOF) is sacrificed due to the tradeoff between the resolution and DOF. In addition, a large aperture of the focused transducer is undesired for implementation of a miniature PAE probe. PAE with high resolution over large DOF is still a challenge to be addressed.

Synthetic aperture focusing technique (SAFT) is a method to improve the degraded lateral resolution to equivalently extend the DOF. SAFT has been widely employed in acoustic-resolution photoacoustic microscopy (AR-PAM) with linear scanning [13, 14], and more recently with mirror-based arc scanning [15]. In addition, SAFT has been explored for endoscopic imaging. For example, in ultrasound endoscopy with circular scanning, SAFT has long been exploited to improve the transverse resolution [16,17]. As for PAE, SAFT has been used to improve resolution for forward-viewing PAE [18]. Compared with the forward-viewing PAE, side-viewing PAE is of its clinical value by being able to observe the whole sidewall along human internal passages such as the coronary artery, the esophagus, and the trachea.

In this work, for the first time to our knowledge, we explore SAFT for side-viewing PAE with

mirror-based scanning to simultaneously enable high resolution, deep penetration, and large DOF. We first perform numerical simulation to optimize the probe design of side-viewing PAE. The probe design involves the placement of a point-like ultrasonic detector and the diameter of a reflection rod mirror. The ultrasonic detector used in the numerical simulation has an active area of 10 μm [19] and a bandwidth of 20 MHz [19, 20]. A PAE probe is then constructed based on the optimized design. A home-built fiber-tip Fabry-Perot (FP) ultrasonic detector [19] is employed. The point-like ultrasonic detector ensures a wide detection angle and thus a large synthetic aperture for SAFT. Imaging of 50 μm tungsten wires demonstrates the full width at half maximum (FWHM) transverse resolutions of 115–190 μm at a radial distance of 2–5.5 mm (i.e., DOF of 3.5 mm). The efficacy of SAFT in side-viewing PAE is further validated by three-dimensional (3D) phantom imaging.

2. Methods

2.1. Principles of photoacoustic imaging

As described in literature [21], photoacoustic pressure $p(\mathbf{r}, t)$ at position $\mathbf{r}$ and time t generated in an acoustically homogeneous and non-viscous medium is expressed as

$$\nabla^2 p(\mathbf{r}, t) - \frac{1}{c^2} \frac{\partial^2}{\partial t^2} p(\mathbf{r}, t) = -\frac{\beta}{C_p} \frac{\partial}{\partial t} H(\mathbf{r}, t). \tag{1}$$

In the above wave equation, c is the sound speed in the medium, β denotes the thermal coefficient of volume expansion, C_p stands for the isobaric specific heat capacity, and $H(\mathbf{r}, t)$ is the heating function defined as the thermal energy converted at $\mathbf{r}$ and t per unit volume and time. Heating function is the product of spatial absorption function $A(\mathbf{r})$ and irradiation pulse $I(t)$ as $H(\mathbf{r}, t) = A(\mathbf{r})I(t)$. Under the assumption that $I(t) \approx \delta(t)$, where $\delta(t)$ represents a delta function, we get the initial pressure $p_0(\mathbf{r})$ inside the object as $p_0(\mathbf{r}) = \Gamma A(\mathbf{r})$, where Γ is the Grueneisen coefficient. If the object is in a spherical shape with a radius of a and is uniformly illuminated by a delta laser pulse, the analytical solution for the acoustic pressure, at $\mathbf{r}_0$ (usually representing the positions of ultrasonic detectors) and time t, emitted from this spherical object is

$$p_\delta(\mathbf{r}_0, t) = A_0 U(a - |r - v_s t|)(r - v_s t)/(2r), \tag{2}$$

where A_0 is the amplitude of the initial pressure, r is the distance from the center of the object to $\mathbf{r}_0$, and $U(\xi) = 1$ for $\xi \geqslant 0$ and $U(\xi) = 0$ otherwise. In practice, the detected photoacoustic pressure by a point ultrasonic detector can be expressed as the convolution of multiple functions [22]

$$p(\mathbf{r}_0, t) = p_\delta(\mathbf{r}_0, t) \otimes I(t) \otimes L(t) \otimes D(t) \tag{3}$$

where $L(t)$ accounts for the ultrasound propagation loss in the medium, $D(t)$ is the impulse response of the ultrasound detector, and $\otimes$ represents convolution operator. The detected signal can be then used to reconstruct the original light-absorbing object [23].

2.2. Synthetic aperture focusing technique

SAFT has long been utilized to improve the lateral resolution of AR-PAM using a needle hydrophone [13] or a high-NA focused transducer as a virtual-point detector [14]. Linear scanning of ultrasonic detectors is used in the above works. In addition, mirror-based arc scanning for SAFT has also been tested [15]. In fact, SAFT can be applied in arbitrary scanning paths as long as the detection patterns of ultrasonic detectors at adjacent positions along the scanning path are overlapped.

In PAE as illustrated in Fig. 1(a), the ultrasonic detector is placed inside the probe and a reflection rod mirror is placed at the distal end of the probe to realize side-viewing imaging.
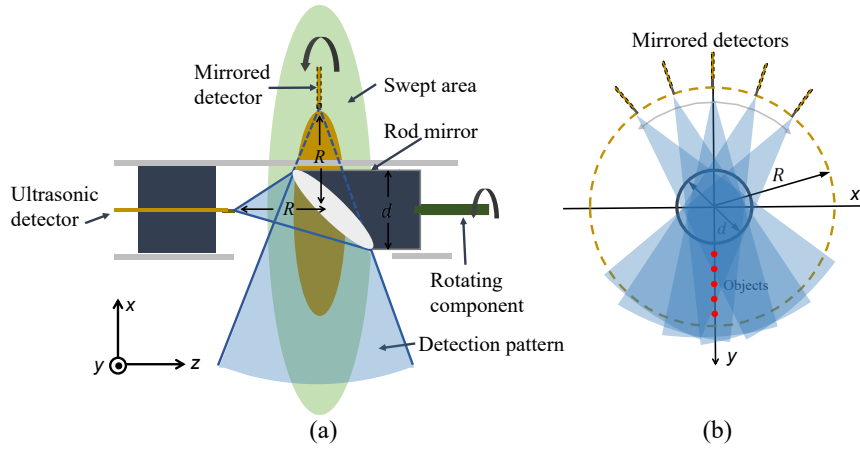
Fig. 1. (a) Schematic of the SAFT-based PAE probe. The rod mirror reflecting the detection pattern of ultrasonic detector is rotated to perform circumferential scanning. The diameter of the rod mirror is d and the scanning radius of the mirrored detector is R. (b) Equivalent scanning path. The overlapped detection patterns of the mirrored detectors facilitate SAFT implementation.

The distance between the tip of the point-like ultrasonic detector and the center point of the reflection rod mirror is denoted by R, and the diameter of the reflection rod mirror is d. To acquire a circumferential image, the reflection rod mirror is rotated while other components are kept stationary. Equivalently, the ultrasonic detector is placed at its mirrored positions and follows a circular scanning path as illustrated in Fig. 1(b). The mirrored detector is circularly scanned with a radius of R. In practice, the objects should be located outside the probe, as shown in Fig. 1(b), and the mirrored detectors on the opposite side of the objects will be used for SAFT. The overlapped detection patterns of the ultrasonic detector at the adjacent positions along a circular scanning path facilitate the implementation of SAFT, which synthesizes a large aperture for focusing by properly delaying and summing the photoacoustic signals received at the adjacent scanning positions:

$$S_{SAFT}(t) = \sum_{i=0}^{N-1} S(i, t - \Delta t_i), \tag{4}$$

where $S(i, t)$ is the photoacoustic signal detected at the scanning position i, Δt_i is the time delay applied to the signal received at the scanning position i. N denotes the total number of adjacent scanning lines included in SAFT summation and is determined by the angular extent of the ultrasonic detection pattern as well as the scanning geometry. In conventional linear scanning, the ultrasonic detection pattern is solely determined by the angular extent (or view angle) of the ultrasonic detector. Note that as for the mirror-based circular scanning in Fig. 1(a), the ultrasonic detection pattern is not only associated with the detector's angular response but is also affected by the finite diameter of the reflection rod mirror d and the distance R.

In addition to SAFT, the focusing quality of SAFT images can be further improved by coherence factor (CF) defined as

$$CF(t) = \frac{|\sum_{i=0}^{N-1} S(i, t - \Delta t_i)|^2}{N \sum_{i=0}^{N-1} |S(i, t - \Delta t_i)|^2}. \tag{5}$$

CF is a real quantity ranging from 0 to 1. After applying the CF map to the SAFT image pixel-by-pixel, the sidelobes in the SAFT image are suppressed and the signal-to-noise ratio (SNR) will also be improved assuming uncorrelated and additive noise.

3. Probe design

SAFT can synthesize a large aperture and then improve the resolution by numerical focusing. For circular scanning PAE, the improved transverse resolution is determined by the NA of the synthetic aperture that can be used in SAFT reconstruction. The NA for circular SAFT is determined by the diameter of the scanning mirror d and the scanning radius R, as will be discussed later. Moreover, small diameter of the mirror is desired for the miniature PAE probe. Both the resolution improvement and the probe size should be taken into account in the optimized probe design of SAFT-based PAE. Thus, we perform numerical simulation by considering the scanning radius R and the diameter of the reflection rod mirror d subject to

$$d < 3.7 \text{ mm.} \tag{6}$$

The constraint limits the diameter of the reflection rod mirror d, which is set because the probe, after encapsulation, should be held in the instrument channel (typically ~3.7 mm in diameter) of a standard video endoscope.

We use the home-built FP ultrasonic detector on the fiber tip in both simulation and experiment [19]. The FP ultrasonic detector has the advantages of good sensitivity, wide bandwidth and easy for miniaturization and has been widely used as a miniature detector for endoscopy. The FP detector is usually considered as a low-pass point detector with its angular response described by

$$d(\theta) = J_1(ka \sin(\theta))/(ka \sin(\theta)), \tag{7}$$

where $J_1(x)$ is the first order Bessel function of the first kind, $k = \omega_a/c$ is the wavenumber of the incident acoustic wave (ω_a: frequency of the acoustic wave; c: sound speed), a is the average radius of active area for detection, and θ is the incident angle of the acoustic wave [24]. In our simulation, $L(t)$ in Eq. 3, which is mainly due to water absorption, has an attenuation coefficient of 2.2×10^{-4} dB/(mm· MHz^2) [25]. As for $D(t)$ in Eq. 3, the FP detector with −6 dB bandwidth of 20 MHz and an active area of 10 μm in diameter [26] is considered.

For the given FP ultrasonic detector, we seek the optimized probe design in numerical simulation by studying the dependence of transverse resolutions on the diameter of the reflection rod mirror d and the scanning radius R. The diameter of rod mirror is set as 1–4 mm. For each case of d, scanning radii $R = 1$–5 mm are numerically simulated. We then check the transverse resolutions after SAFT+CF for the objects at radial distance of 1.5 –5.5 mm from the rotating axis of the probe to find the optimized probe design. Note that the cases with $d > 3.7$ mm will not be considered although simulated, as mentioned above.

Transverse resolutions after SAFT+CF for each case of (d, R) are shown in Fig. 2. The farther the object from the rotating axis of the probe, the worse the transverse resolution will be after SAFT. For $d = 1$ mm in Fig. 2(a), the transverse resolutions are 100–500 μm regardless of the scanning radius. The reflection rod mirror with diameter of 1 mm greatly limits the detection pattern of the FP detector and thus, restricts resolution improvement of SAFT. As d increases, the transverse resolutions become better than those of $d = 1$ mm as presented in Figs. 2(b)–(d). From the results, the best transverse resolutions are achieved for the case of $d = 4$ mm and $R = 3$–5 mm. However, due to the constraint that $d < 3.7$ mm, we thus choose $d = 3$ mm in our probe design. Furthermore, the resolution curves in Fig. 2(c) show difference for different scanning radii. The case of $R = 1$ mm is obviously excluded. The resolutions for $R = 3, 4$, and 5 mm are basically the same and are slightly better than those for $R = 2$ mm. Finally, as a result, we choose $d = 3$ mm and $R = 4$ mm as the optimized probe design.

4. Results

We construct the PAE probe to validate our simulation results using a 3-mm-diameter reflection rod mirror (#54-094, Edmund). Figure 3 shows the photograph of the PAE probe. The ultrasonic detector employed is a home-made fiber-tip FP detector which has an active area of ~10 μm.
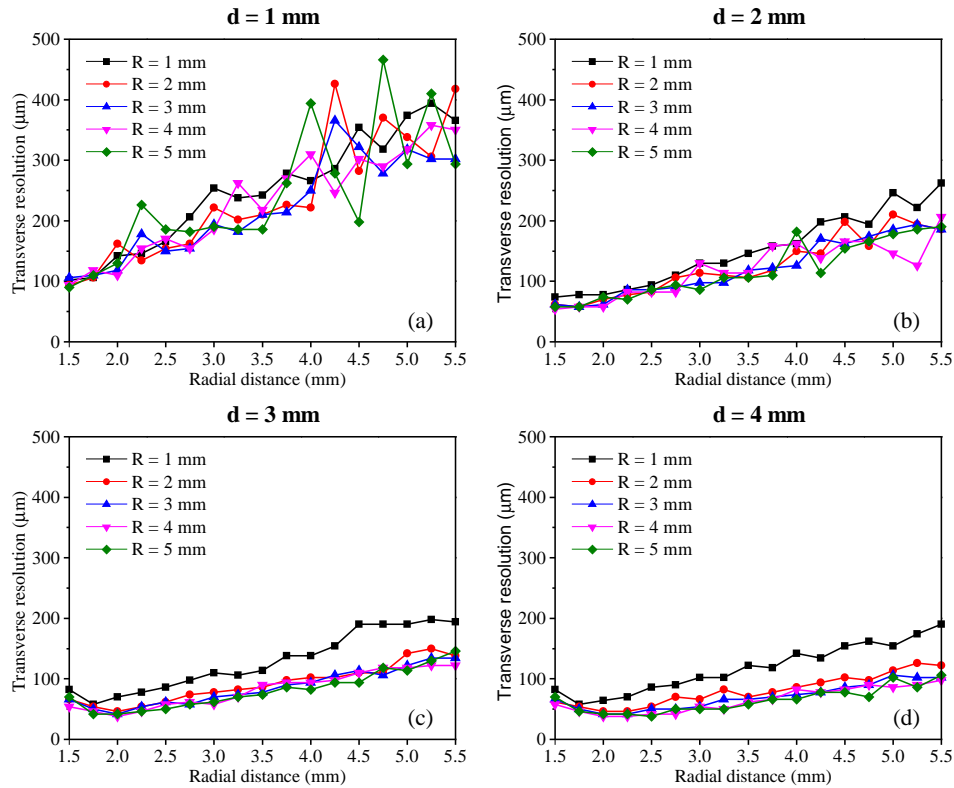
Fig. 2. Numerical simulation of transverse resolutions by SAFT+CF for (a) *d* = 1 mm, (b) *d* = 2 mm, (c) *d* = 3 mm, and (d) *d* = 4 mm. For each case of *d*, scanning radii *R* = 1–5 mm are numerically simulated.
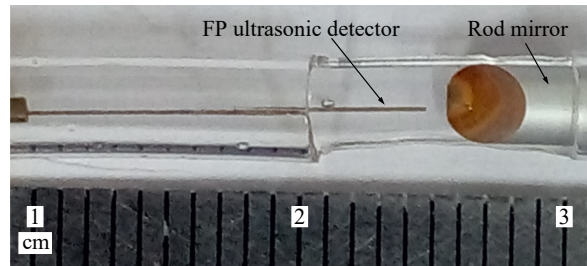

Fig. 3. Photograph of the PAE probe with the optimized design.

4.1. Resolution calibration

We use 50-μm tungsten wires to perform resolution calibration. The tungsten wires are placed from 2 mm to 5 mm in radial distance with 0.5 mm separation. Light is illuminated uniformly from the outside of the probe. Circumferential scanning is performed by a rotary motor with a step angle of 1.8°. For every angular position, the photoacoustic A-line signal is sampled at 500 MS/s with an oscilloscope (WaveSurfer 3034, Teledyne LeCroy). The A-line signal is averaged 16 times and a digital low-pass filter with a cutoff frequency of 30 MHz is further applied to the signal for SNRs improvement.

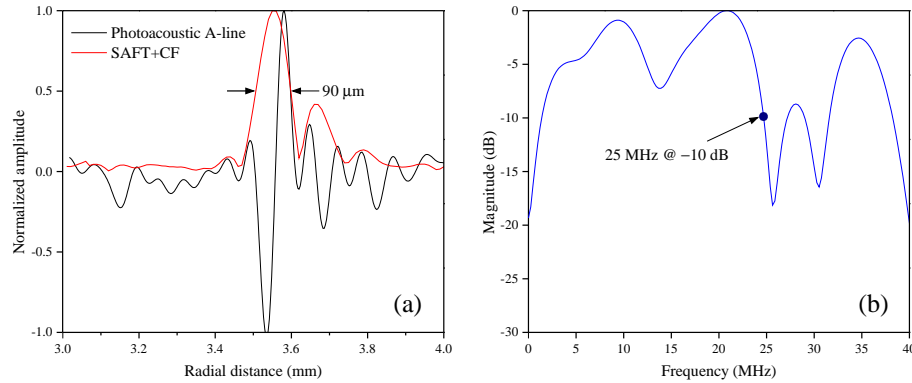The radial resolution of SAFT-based PAE is provided by the time-resolved ultrasonic detection

Fig. 4. (a) FWHM radial resolution in SAFT+CF image is 90 µm. (b) Frequency response of the FP ultrasonic detector used in experiment.

and is inversely proportional to the ultrasonic detector's bandwidth. The object located at a representative radial distance of 3.5 mm is checked. The FWHM radial resolution in the SAFT+CF image (shown later) is 90 µm as shown in Fig. 4(a). Figure 4(b) shows the measured non-ideal frequency response of the FP detector used in this experiment, with a -10 dB point at 25 MHz.
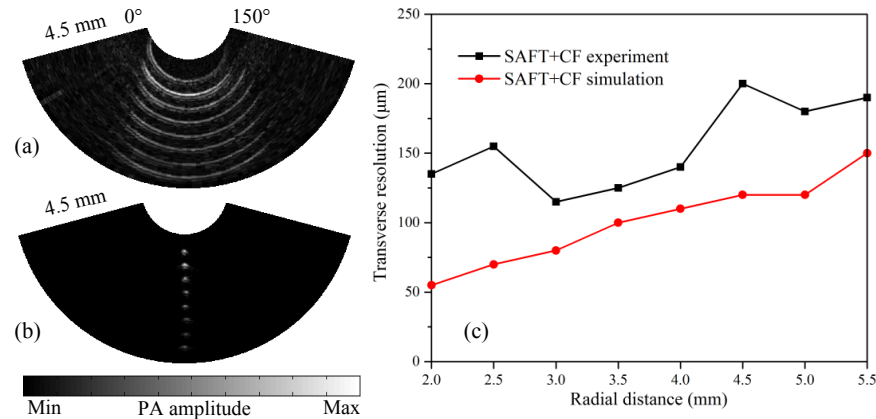

Fig. 5. Transverse resolution calibration: (a) Original image. (b) SAFT+CF image. (c) Transverse resolutions vs. radial distance for experimental SAFT+CF (black curve) and simulated SAFT+CF (red curve) images.

The original image without applying any reconstruction algorithm shows wide transverse extent in Fig. 5(a) due to the wide angular response of the FP detector. After applying SAFT+CF reconstruction (Fig. 5(b)), we obtain high transverse resolution of 115–190 µm in an imaging depth range of 3.5 mm. Note that the transverse resolutions after SAFT degrade as the radial distance increases, which is different from the uniform lateral resolutions along the depth direction in linear SAFT. The improved transverse (or lateral) resolution is determined by the NA for SAFT. For linear SAFT, objects at different depths have almost the same NA for SAFT, and thus, SAFT provides uniform lateral resolution along the depth direction. In contrast, for the circular SAFT for PAE in this work, objects at shallow radial positions have a large NA for SAFT while those at deep radial positions have a low NA for SAFT, as shown in Fig. 1(b) , due to the inherently geometric characteristic of the circular scanning for PAE.

Simulated and experimental transverse resolutions for the SAFT+CF image are plotted in Fig. 5(c) for comparison. For better comparison, the measured frequency response in Fig. 4(b) is used in this simulation. The discrepancy between the simulation and experimental results is in part caused by the difference in the angular responses of the FP detector used in simulation and in experiment. A theoretical angular response as described by Eq. 7 is assumed in simulation, while an actually irregular angular response is used in experiment. The calibrated irregular angular response will be presented in our another recent work. In addition to improving the transverse resolution, the SNR in the SAFT+CF image is also improved by taking advantage of the signal averaging property of SAFT and CF.

To better demonstrate the advantage of high transverse resolution over a large imaging depth range achieved by SAFT-based PAE, we compare the transverse resolution and imaging depth range of different PAE schemes in Table 1. OR-PAE [7, 8, 12] provides high transverse resolution of 10–20 μm by optical focusing in a very limited imaging depth range (< 0.5 mm). AR-PAE using an unfocused transducer [9, 11] has larger imaging depth at the cost of degraded transverse resolution of 200–400 μm. On the other hand, AR-PAE using a focused transducer [2, 10] enables higher transverse resolution of 100–200 μm, yet the imaging depth range is limited by the DOF of the focused transducer to ~2 mm. Currently, our SAFT-based PAE achieves comparable transverse resolution (115–190 μm) to that of AR-PAE using a focused transducer (100–200 μm), while the former has larger imaging depth range (> 3.5 mm) than the latter (~2 mm). That is, our SAFT-based PAE improves the imaging depth range by more than 1.7 times compared with AR-PAE using a focused transducer. Although the focused transducer has better detection sensitivity than the point-like FP ultrasonic detector for single detection of photoacoustic A-line signals, the latter employs SAFT to improve SNR and thus, SAFT-based PAE is still able to provide decent sensitivity comparable to that of AR-PAE using a focused transducer.

Table 1. Transverse resolution and imaging depth range of different PAE schemes

PAE schemes	Technologies	Transverse resolution (μm)	Imaging depth range (mm)	Refs.
OR-PAE	Optical focusing	10–20	< 0.5	[7, 8, 12]
AR-PAE	Unfocused transducer	200–400	~2.5	[9, 11]
	Focused transducer	100–200	~2	[2, 10]
SAFT-based PAE	SAFT reconstruction	115–190	> 3.5	This work

Note that the FP detector used in this study has the non-ideal frequency response and angular response, leading to worse transverse resolution in experiment, as shown in Fig. 5(c). Further development of the FP detector is helpful to achieve better transverse resolution. Moreover, broader bandwidth of the ultrasonic detector can further improve the transverse resolution. Microring ultrasonic detectors with ultrabroad bandwidth may be potential candidates for SAFT-based PAE [27, 28]. In this regard, SAFT-based PAE has potential to achieve high transverse resolution up to tens of micrometers over large DOF of > 3 mm.

4.2. 3D phantom imaging

To better illustrate the efficacy of SAFT for PAE, 3D phantom made of four human hairs with different orientation and positions was imaged. Circumferential scanning was performed on the *xy* plane with the reflection rod mirror and a relatively slow mechanical scanning was performed with a motorized translation stage along the *z* axis. A step angle of 1.8° was adopted in the circumferential scanning. To enlarge the imaging region and to reduce the total scanning time, a step size of 100 μm in the mechanical scanning was used with a 3-mm scanning range along the

z direction. After obtaining the original volumetric data, the data was interpolated by a factor of 2 along the z direction to equivalently reduce the step size to 50 μm.
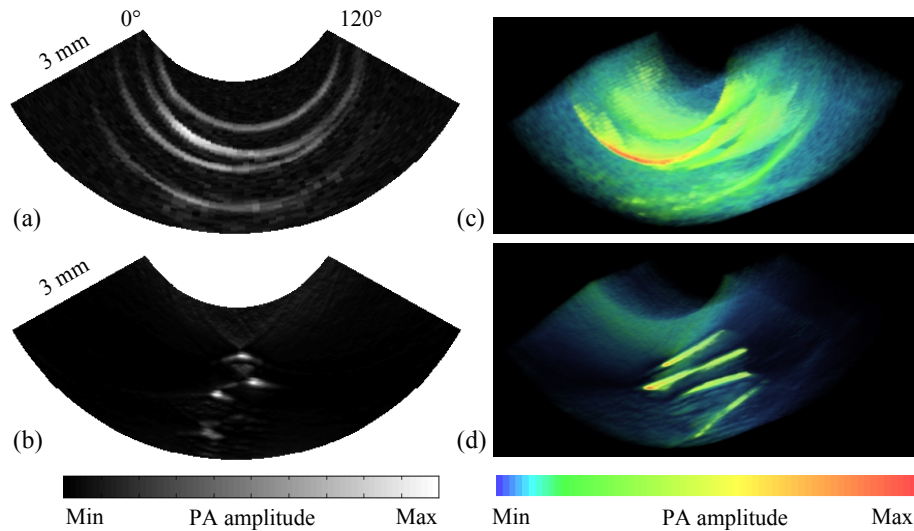

Fig. 6. Cross-sectional B-mode image at $z = 2$ mm for the (a) original and (b) SAFT+CF images, respectively. Volumetric rendering images of the human hair phantom for the (c) original and (d) SAFT+CF images, respectively. Animations of B-mode images along the z axis are available as supplementary visualization for the original image (see Visualization 1) and the SAFT+CF image (see Visualization 2).

We used two-dimensional (2D) reconstruction slice by slice and combined the slices for 3D imaging. The pixel size on the xy plane for reconstruction is set as 20 μm for both the x and y directions. We check the representative cross-sectional B-mode images at $z = 2$ mm for the original and SAFT+CF cases, as shown in Figs. 6(a) and 6(b), respectively. The SAFT+CF image in Fig. 6(b) can clearly distinguish relative positions of the four hairs due to the high transverse resolution over large DOF. Figures 6(c) and 6(d) show the volumetric rendering images before and after SAFT+CF, respectively. A clear identification of the 3D phantom's location and orientation can be achieved in Fig. 6(d) after performing SAFT+CF on the xy plane. Besides, the background noise is greatly reduced after SAFT+CF which enables better identification of the four hairs.

5. Discussions

The fiber-tip FP ultrasonic detector as a point-like detector has a wide angular response, which facilitates SAFT implementation to synthesize a large aperture. Furthermore, the all-optical PAE probe based on optical detection of ultrasound has the advantage of immunity against electromagnetic interference, which is of clinical significance for endoscopic imaging applications.

Currently, a prototype of the PAE probe is constructed, which is sufficient to demonstrate the proposed idea of PAE by SAFT. For *in vivo* imaging, further development of the probe is needed. First, currently external laser illumination is used. A fiber for pulsed laser delivery should be integrated inside the probe. Second, a common step motor is used to rotate the rod mirror in this study. A miniature component such as a micromotor to realize circular scanning should be encapsulated inside the probe. Third, the scanning speed is presently limited by a low laser pulse repetition rate of 20 Hz. The laser with high pulse repetition rate should be employed for fast imaging. Tissue motion in *in vivo* PAE imaging degrades the SAFT image quality. Fast data acquisition also alleviates, to some extent, the issue of tissue motion during *in vivo* imaging. The diameter of the fully encapsulated probe should be controlled to be less than 3.7 mm so as to

be held in the instrument channel of a standard video endoscope. The FP ultrasonic detector in our PAE probe currently has a noise-equivalent pressure on the order of 1 kPa. Development of high-sensitivity detectors is helpful to improve SNR and imaging speed for *in vivo* imaging applications. Besides SAFT, other algorithms such as back-projection can also be applied to the reconstruction-based PAE for comparison.

In our 3D imaging demonstration, SAFT is performed only on the *xy* plane (i.e., one-dimensional SAFT). 2D SAFT for PAE, which is a cylindrical scanning configuration, is able to improve resolutions in both the transverse and axial directions [29]. In SAFT-based PAE, the improved transverse resolution is determined by the NA for *circular* SAFT, which is affected by the view angle of the mirrored detectors and the available synthetic aperture size, both of which are related to the scanning radius R and have a tradeoff relation for the NA for circular SAFT. Specifically, for the case of a small R, although the view angle of the mirrored detectors is large (large NA for SAFT), the available synthetic aperture size is very limited (small NA for SAFT) compared with a large R. Thus, the optimized R for high transverse resolution should be determined via numerical simulation (as shown in Fig. 2), which shows that an increased R improves the transverse resolution. On the other hand, the axial resolution improvement (z direction in Fig. 1(a)) is determined by the NA for *linear* SAFT, which is solely affected by the view angle of the mirrored detectors. Thus, a small R improves the axial resolution. The optimization of the transverse and axial resolutions is of interest to explore in future.

6.   Conclusions

In summary, we apply SAFT to enable high transverse resolutions over large DOF for side-viewing PAE. Numerical simulation is first performed to optimize the PAE probe design. The probe design involves the placement of the ultrasonic detector, the diameter of the reflection rod mirror, and the optimization of transverse resolution. With the optimized probe design, high transverse resolution of 115–190 μm over large DOF of 3.5 mm is achieved. The efficacy of our PAE probe is further validated by 3D phantom imaging. SAFT-based PAE has the potential to realize fine spatial resolution (tens of micrometers) over large DOF (> 3 mm) given the detector with broader bandwidth, which is of great interest for future development.